Chapter 10
Thermoeletric Heusler Compounds

Julia Krez and Benjamin Balke

Abstract Thermoelectric converters for power generation aim at reducing CO_2 emission via the conversion of a part of the low-grade waste heat generated by engines, industrial furnaces, gas pipes, etc. to electricity. The recovery of waste heat from the exhaust of an automotive engine, in particular, is an attractive, albeit not very efficient way for reduction of fuel consumption. Thermoelectric converters with high overall efficiency convert heat directly into electricity without moving parts and, thus, not only decrease our reliance on fossil fuels but also actively counteract global warming. State-of-the-art converters are simply too inefficient to be economic, partly due to expensive elementary constituents (Te, Ge, etc.). On this background, Heusler compounds with $C1_b$ structure stand out on account of their relatively low cost components and have been extensively studied as potential thermoelectric materials for high temperature power generation up to 1000 K during the last years.

10.1 Introduction

The search for alternative energy technologies has taken an accelerated pace in recent years as climate change has become more noticeable and the use of nuclear energy introduces political controversy for many countries. The quest for sustainable energy sources has piqued interest in different research fields to find new energy conversion techniques to satisfy the worlds rising demand for energy. In 2013 the Lawrence Livermore National Laboratory has suggested that more than the half (i.e. 61 %) of the energy that flows through our economy is ultimately wasted [1]. The most of the energy is dissipated as waste heat and only 25 % is used as mechanical power [2, 3]. Some of this thermal energy could be converted directly into electrical energy by a thermoelectric generator (TEG) [4, 5]. Presently, thermoelectric (TE) devices are

J. Krez · B. Balke (✉)
Institut für Anorganische und Analytische Chemie,
Johannes Gutenberg - Universität, 55099 Mainz, Germany
e-mail: balke@uni-mainz.de

J. Krez
e-mail: krez@uni-mainz.de

actively considered as a clean energy source for waste heat recovery in automobiles, since they operate silently and do not have any moving parts or environmentally harmful fluids. The captured energy can be used for a vehicle's electrical components such as air conditioning, lights and windows without additional engine load [6]. This in turn can make a crucial contribution to an improvement in fuel economy, and thus a reduction of CO_2 emissions. Beside waste heat recovery, thermoelectric (TE) devices have been investigated for their use in TE-solar hybrid systems [4], TE-refrigeration [7] and as radioisotope TEGs for deep-space application of NASAs Voyager and Cassini missions [8].

The pioneer in introducing semiconductors as promising materials for TE application was Ioffe [9, 10]. His work led to a very active period in TE research in the 1950s and early 1960s, when many new TE materials were discovered and investigated. At this time, Goldsmid [11] showed the high potential of Bi_2Te_3 as a TE material, and this material remains the basis for the TE industry up to the present time. Ioffes proposal to employ semiconductor alloys rather than simple binary compounds in order to lower the thermal conductivity lead to todays huge variety of material classes such as skutterudites, clathrates, Half-Heusler compounds and complex chalocogenides as promising candidates for TE application. An extensive overview of all material classes and their TE properties can be found in [12, 13]. Guided by the figure of merit zT, the most promising materials with high zT seems to be narrow band gap semiconductors with heavy elements and complex unit cells.

The theoretical predictions by Hicks and Dresselhaus [14, 15] and later by Slack [16] have stimulated a new wave of interest in complex TE materials, where the realization of new ideas mainly emerges from interdisciplinary collaborations between chemistry, physics and material science. Thus, a materials engineering approach must be pursued to either enhance more established materials or to discover completely new classes of materials. In fact, little enhancement in highly efficient TE materials has been made in the past six decades. The figure of merit of the TE compounds for industrial applications has remained static with zT≈1 for a temperature difference $\Delta T = 300$ K. State-of-the-art converters are simply too inefficient to be economic, partly due to expensive elementary constituents (Te, Ge, etc.). Currently Bi_2Te_3-based TE materials are used for applications from room temperature to 200 °C, for higher temperatures PbTe-based materials are appropriate material choice. Although Bi_2Te_3 and PbTe are high performance TE materials, a general application becomes more difficult, because Te is a rare and the environmentally friendliness of Pb and Bi is questionable.

A commercially available TE module for power generation or cooling, as shown in Fig. 10.1a, consists of many n- and p-doped semiconductors, so called TE elements. Each TE element is connected by metal contacts and is sandwiched between electrically insulating ceramic plates, which are high thermal conductive [5]. It is important that the contact material is rigid and exhibits similar thermal expansion coefficients to avoid contact cracks. The TE elements are connected electrically in series but thermally in parallel, to optimize the heat flow from the hot to the cold end [5]. Considering the Seebeck effect, the temperature gradient drives charge carriers from the hot end to the cold end in the material, where the rejected heat must
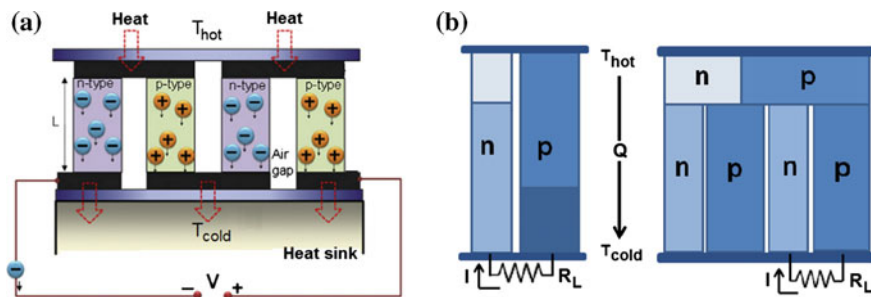
Fig. 10.1 a Illustration of a TE module. **b** Illustration of a segmented TEG (*left*) and a cascaded TEG with a cascading ratio of three (*right*)

be removed by a heat sink. Thus, electrons diffuse from the hot to the cold end in the *n*-type material, and holes in the *p*-type material, respectively.

To break out of the limited applicability of TE devices and realize adoption in other application fields, it is necessary to increase the TE efficiency of a TEG. The theoretical assumption is that doubling of the device ZT up to 2 could lead to a tenfold increase in the number of TE purposes [17]. Therefore, the main efforts in TEG optimization are focused on the materials optimization but also due to the device engineering, e.g. cascaded or segmented generators (see Fig. 10.1b), where the *n*- and *p*-type TE elements (or TE legs) are combined with different materials and joined in series [18]. Ideally, the segmentation helps to improve the TE efficiency, if both materials are operating in their most efficient temperature range. For any TE material to become viable for future applications, it needs to fulfill a set of criteria (see Fig. 10.2), beyond those of being an efficient TE material. A commercial and nationwide application a of TE material has to meet the requirements of being non-toxic, cheap and earth abundant, mechanically and thermally stable and furthermore provide the possibility of processable and reproducible high volume manufacturing. On this background, Heusler compounds with $C1_b$ structure stand out on account of

Fig. 10.2 Illustration of the criteria for TE materials required for large-scale power generation
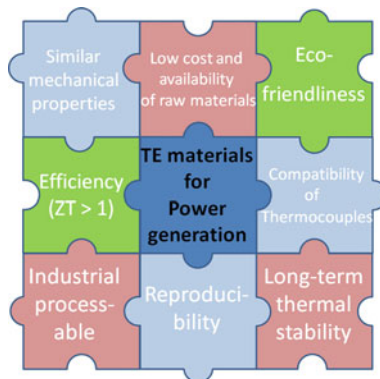
their relatively low cost components and have been extensively studied as potential thermoelectric materials for high temperature power generation up to 1000 K during the last years.

This book chapter will give an overview about the research on Heusler compounds for thermoelectric applications during the last decade. Since there are already a lot of reviews concerning several nano approaches [19–22], this chapter will focuss on phase separation as a key to highly efficient thermoelectric Heusler compounds and illustrate the possibility of designing a thermoelectric material pair of almost the same material.

10.2 Structure and Production of Thermoelectric Heusler Compounds

Half-Heusler (HH) compounds with the general formula XYZ (X, Y = transition metal, Z = main group element) crystallize in a non-centrosymmetric cubic $C1_b$ structure ($F\bar{4}3m$, spacegroup 216), [23, 24] shown in Fig. 10.3, are in focus of the present thermoelectric research, since they fulfill almost all requirements for a commercial applications [19, 25–45]. Their mechanical and thermal stability is exceptional in comparison to the commonly used thermoelectric materials [46]. The possibility to substitute small amounts of elements from the parent compound without destructing the lattice structure allows tuning the electronic properties [47, 48]. This tunability also allows to avoid the use of toxic and expensive elements. The reported thermoelectric Heusler compounds exhibit high electrical conductivity and moderate values of the Seebeck coefficients, which lead to a high powerfactor [37].

HH compounds contain high melting point elements such as Hf: 2231 °C, Zr: 1855 °C, Ti: 1668 °C, Ni: 1455 °C, and Co: 1495 °C as well as elements with relatively low melting point such as Sn: 232 °C and Sb: 631 °C. Therefore, a high temperature alloying method is necessary. Usually, this is done by stoichiometric weighting the constituting elements, followed by arc-melting in an Ar atmosphere for at least three times using a home-made or a commercial system. After this the samples are crushed and remelted, to insure the homogeneity of the samples. Other preparation techniques for HH compounds are usually induction heating [31], solid state reaction [45] or new preparation techniques as melt spinning [49] or spark plasma sintering (SPS) [34, 50].

Usually, an additional heat treatment is necessary for all samples to obtain the $C1_b$ structure and to eliminate possible secondary phases which could occur during the melting process. Typically, this annealing of the ingots is done under vacuum in quartz ampules between 900 °C and 1050 °C for 3 to 7 days, followed by quenching them in ice water. Since the industrial application of a product is always as well a matter of the price, one important task for the ongoing thermoelectric research is to identify the minimum necessary annealing time while preserving a high figure of merit zT. For more details about all the possibilities, opportunities, and challanges
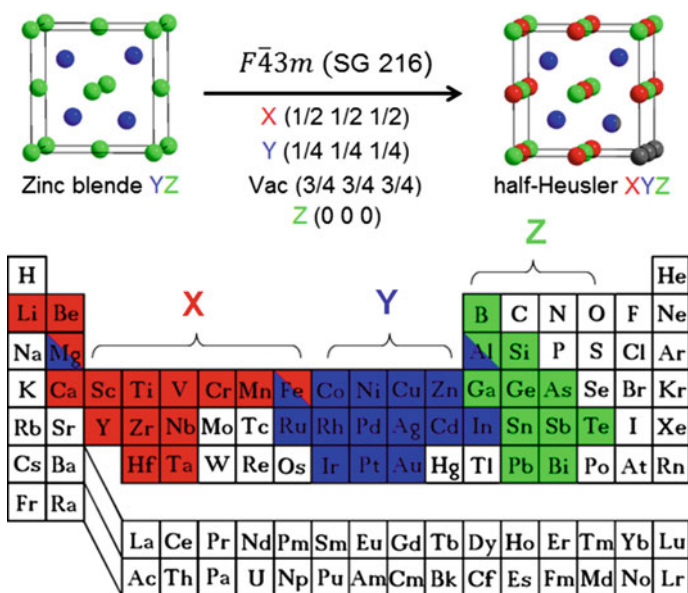
Fig. 10.3 Periodic table of elements including the crystal structure $F\bar{4}3m$ of zinc blende and HH compound. The various number of HH compounds can be formed by combination of the different elements according the color scheme

concerning the production of HH compounds see [27]. A relatively new approach is using an energy and time-efficient process involving solid-state preparation in a commercial microwave oven [38, 51].

Even though one can read quite often that mechanical alloying (MA) of HH compounds of the elements is not successful due to limited energy input and the high melting points, usually the [52] is cited, this might be true for NiTiSn-based compounds but for sure is not the case for CoTiSb-based compounds. Using a high energy ball mill (Fritsch *Planeten-Mikromühle PULVERISETTE 7 premium line*) we succeed with the mechanical alloying of several state-of-the-art *p*-type HH compounds such as TiCoSb, HfCoSb, ZrCoSb, $TiCo_{0.85}Fe_{0.15}Sb$, $TiCo_{0.7}Fe_{0.3}Sb$, $Zr_{0.5}Hf_{0.5}CoSb_{0.8}Sn_{0.2}$, and $ZrCoSb_{0.9}Sn_{0.1}$. Exemplary for all those HH compounds, the results on the MA of $TiCo_{0.85}Fe_{0.15}Sb$ are described in more details. Figure 10.4d shows the x-ray diffraction (XRD) patterns of the as-milled $TiCo_{0.85}Fe_{0.15}Sb$ HH nanoparticles as a function of milling time. After milling for more than 6 h, the HH phase appears. Longer milling, however, results in some impurity phase (for example, as the case of 20 h). Transmission Electron Microscope (TEM) investigations reveal the size of Heusler nanoparticles is around 15 nm (see Figs. 10.4a,b). Mechanical ball milling method is a top-down based method and is facile to scale up. Heusler nanoparticles produced by this approach, however, are easily agglomerated, severely strained, presented with numerous intermediate phase. For a very recent review about Heusler nanoparticles see [53]. Bartholomé et al. built thermoelectric modules based
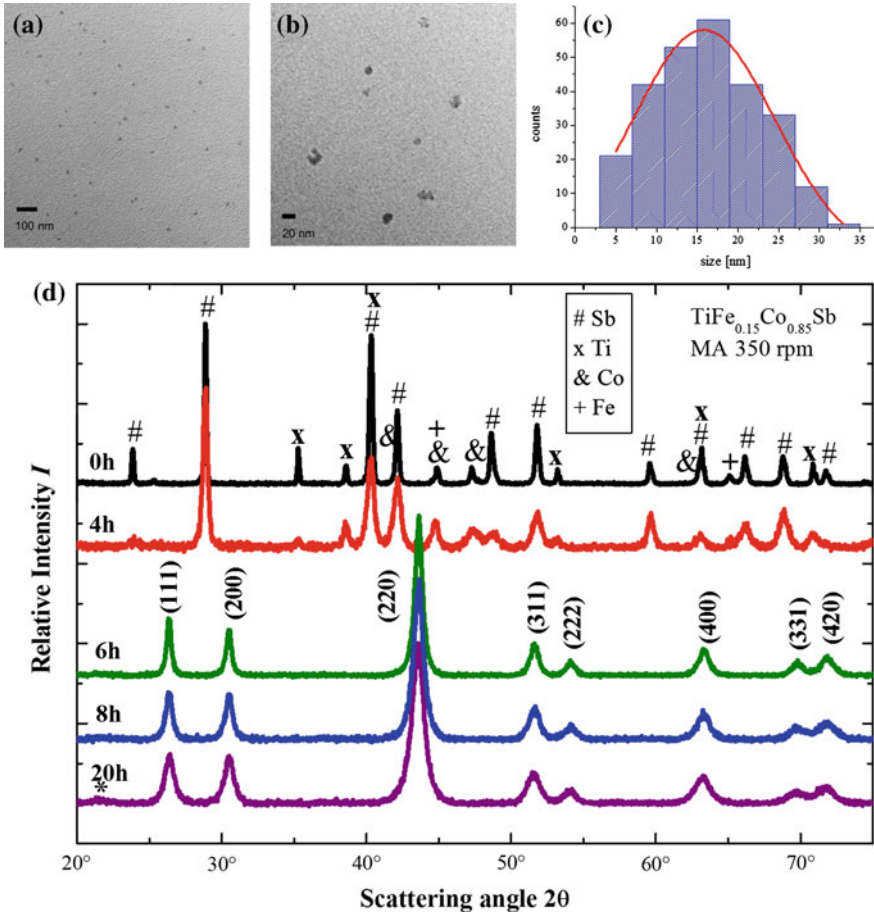
Fig. 10.4 Exemplary TEM micrographs **a b**, and the corresponding histogram **c** for a $TiCo_{0.85}Fe_{0.15}Sb$ nanoparticle sample milled for 8h with 700 rpm. **d** XRD patterns as a function of milling time for as-milled (350 rpm) $TiCo_{0.85}Fe_{0.15}Sb$ nanoparticles. For comparision the XRD result of the mixture of the elemental powders before milling is shown

on HH compounds from material synthesized in kg-batches [31]. The material performance is in line with the published values for comparable material compositions and exhibits peak ZT-values of 0.7 for the n-type and 0.5 for the p-type samples. The modules built from these materials have a maximum power output of 2.8 W with a total module area of $16 \times 16\,mm^2$, resulting in the highest values for the power density of $3.2\,W/cm^2$ and a Z-value of $3.1 \times 10^{-4}\,K^{-1}$ for HH modules published so far. The long-term stability and reproducibility of these modules could be verified by the authors.

10.3 Electronic Structure of Thermoelectric Heusler Compounds

According to the literature, both n-type compounds with the elemental formula MNiSn (M = Ti, Zr, Hf) and p-type MCoSb display a high potential for exceptional ZT values. Research has, therefore, focussed mainly on improvement of these ternary intermetallic compounds. Figure 10.5 shows the calculated band structure (a) and the density of states (b) of NiTiSn. The compound is a semiconductor with an indirect gap. The valence band maximum appears at Γ and the conduction band minimum at X. The band gap has a size of $\Delta E_{gap} = 0.45\,\text{eV}$. The optical gap at Γ is considerably larger ($\Delta E_\Gamma = 1.38\,\text{eV}$).

The electronic structure exhibits at $5\,\text{eV}$ to $8\,\text{eV}$ below the Fermi energy the typical sp hybridization gap that separates the low lying a_1 (s) from the t_1 (p) bands. The high density of states at about $-2\,\text{eV}$ emerges mainly from Ni d states. The high density of states at $-0.7\,\text{eV}$ arises mainly from Ni d states with e symmetry. Most important for the transport properties, the states at both band edges are due to Ti d states with t_2 symmetry. From the band structure shown in Fig. 10.5 it is obvious that electron (n) or hole (p)doping will have rather different results. It is easily seen that p-type doping creates holes in the triply degenerate valence band at Γ whereas the situation is completely different for n-type doping that fills electrons into the single conduction band above the indirect gap at X.

For comparision, Fig. 10.5c,d shows the calculated band structure and the density of states of CoTiSb. The topmost valence band at ϵ_F of the semiconducting pure CoTiSb has t_2 character at the Γ point that has T_d symmetry. It is followed by d bands of e ($-1.56\,\text{eV}$) and bands of t_2 ($-2.39\,\text{eV}$) character. The low lying a_1 states are found below $-9.4\,\text{eV}$ and are separated from the higher lying bands by the sp hybridization gap that is typical for Heusler compounds. The pure CoTiSb exhibits an indirect $\Gamma - X$ band gap of about $1.06\,\text{eV}$, whereas the optical gap at Γ is considerably larger ($1.83\,\text{eV}$). Both, topmost valence band and lowest conduction band appear very low dispersing with a bandwidth of $\approx 150\,\text{meV}$ in the $\Gamma - L$ direction and
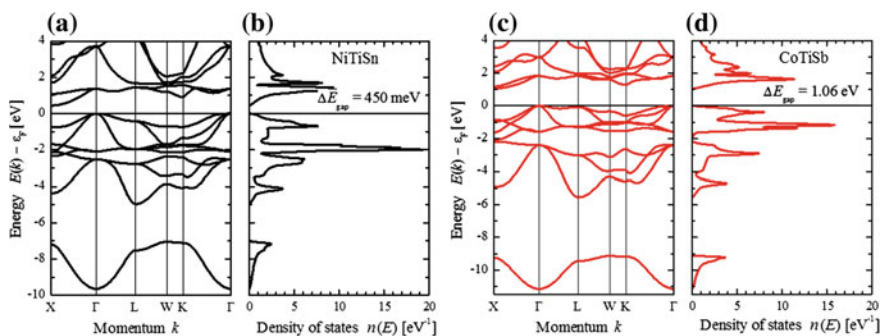

Fig. 10.5 Electronic structure of NiTiSn **a b** and CoTiSb **c d**

thus allow easily for direct optical transitions at energies of about 1.8 eV. For more details about this electronic band structure calculations see [54, 55]. Miyamoto and coworkers studied the electronic structures of the Heusler compounds MNiSn by means of photoelectron spectroscopy [56]. They observed "in gap" states close to the Fermi edge and suggested that these electronic states are mainly created by chemical disorder, which could be the key to control the thermoelectric properties. For more details about this "in gap" states see [54, 55, 57].

In order to achieve the best performance of thermoelectric module the $n-$ and $p-$ type materials to be used should be designed to exhibit similar chemical and physical properties [58]. This can be easily realized when starting from the same material, e.g. the Heusler compound NiTiSn. Yang and coworker evaluated theoretically the thermoelectric-related electrical transport properties of several Heusler compounds, they calculated the maximum power factors and the corresponding optimal $n-$ or $p-$type doping levels [59], which can provide guidance to experimental work. Horyn and coworkers investigated the effect of a partial substitution of Ti and Zr by Sc on the thermoelectric properties of MNiSn-based compounds and obtained at room temperature a fairly high positive Seebeck coefficient of about 121 μV/K with 5 % Sc substitution of Zr [60].

In the commonly used one-parabolic-band approaches $n-$ or $p-$type doping lead to rather similar results, just with opposite signs for the Seebeck coefficient. The situation in practical materials is more difficult. Depleting the valence band or filling the conduction band acts on electronic states with rather different characters. Starting from the calculated electronic structure, the transport properties are calculated using Boltzmann transport theory [61]. Doping the semiconducting materials by electrons or holes will change the transport properties. The doping will cause the chemical potential to change its position. At high doping levels it will shift into the valence band (hole doping) or conduction band (electron doping). Figure 10.6a, b show the calculated Seebeck and power coefficients as function of the position of the chemical potential, respectively. The calculations were performed for NiTiSn and for $T = 300$ K. It is assumed that the shift $\delta\mu = 0$ corresponds to the middle of the band gap at $T = 0$. The Seebeck coefficient exhibits the typical semiconductor behavior under doping, it is positive for hole and negative for electron doping. It is largest for small shifts of the chemical potential from the original position. At 300 K it is already slightly positive in the middle of the band gap. the Reason is the shift of the chemical potential with temperature $\mu = \mu(T)$ to ensure charge neutrality of the system when no voltage is applied. At 300 K the shift amounts to $\delta\mu \approx 13$ meV. The size and direction of the shift depends on the shape of the valence and conduction bands. For applications, the power factor $PF = S^2\sigma$ is more interesting than the Seebeck coefficient alone. The power coefficient, as shown in Fig. 10.6b, is defined here by the power factor divided by the relaxation time τ. The reason for this is that the calculations deliver σ/τ rather than directly the pure conductivity. The largest power coefficient appears for hole doping when the chemical potential is already shifted slightly outside of the band gap into the valence band. The maximum for electron doping is smaller and also appears when μ is slightly shifted outside of the gap. The reason for this is in both cases the high conductivity when the compound
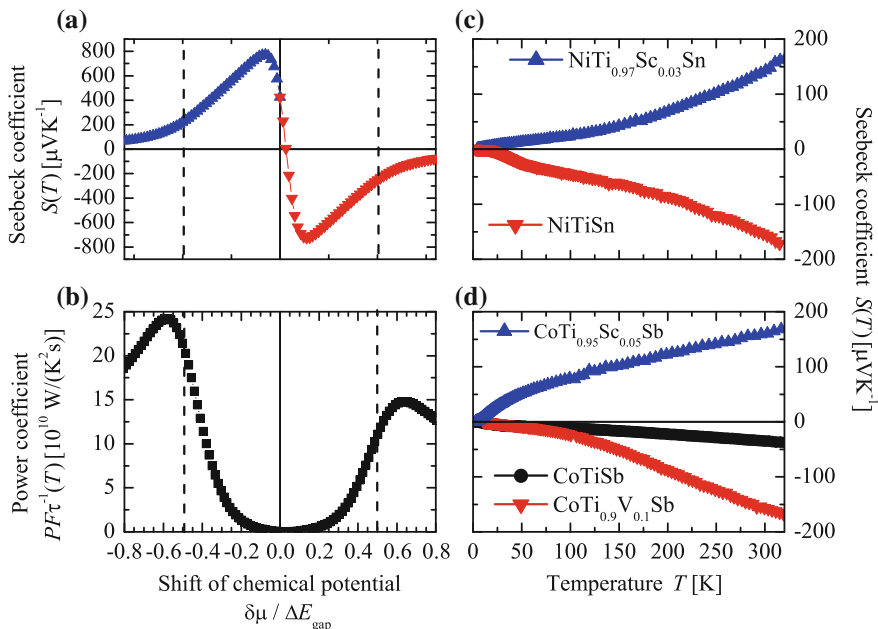
Fig. 10.6 Calculated Seebeck **a** and power coefficients **b** of NiTiSn for $T = 300$ K. The shift of the chemical potential is given with respect to the size of the gap. The valence and conduction band extrema are marked by *dashed lines*. Temperature dependence of the Seebeck coefficient $S(T)$ of NiTiSn and NiTi$_{0.97}$Sc$_{0.03}$Sn in **c** and of CoTiSb, CoTi$_{0.95}$Sc$_{0.05}$Sb and CoTi$_{0.9}$V$_{0.1}$Sb in **d**

goes over into the completely metallic state. From the integrated density of states it is estimated that the maxima of the power coefficient are reached at an electron or hole doping of about 1.1 % or 1.4 %, respectively.

Substituting Ti by V or Sc will act as electron or hole doping, respectively. The difference in the number of valence electrons is in both cases one, such that a substitution by an amount x changes the electron concentration also by $\pm x$. Exemplary, Fig. 10.6c, d show—in full agreement with the calculations—the temperature dependence of the Seebeck coefficient $S(T)$ of pure NiTiSn compared to the substituted compound NiTi$_{0.97}$Sc$_{0.03}$Sn in (c) and of pure CoTiSb compared to the substituted compounds CoTi$_{0.95}$Sc$_{0.05}$Sb and CoTi$_{0.9}$V$_{0.1}$Sb in (d). This shows the possibility to create $n-$ and $p-$type thermoelectric materials based on the same basic compound and thus to produce suitable, well matched pairs for thermoelectric devices out of HH materials. Thus, the probability of cracks and material distortion in the TE device can be reduced and better TE efficiencies can be attained under operating conditions.

The site substitution is mainly used to reduce the thermal conductivity due to an enhanced disorder scattering of phonons [62, 63]. In addition to the reduction of the thermal conductivity, site substitution with non-isoelectronic elements significantly affects the transport properties in HH materials, owing to a shift of the chemical potential. The size and direction of the shift depends on the shape of the valence and
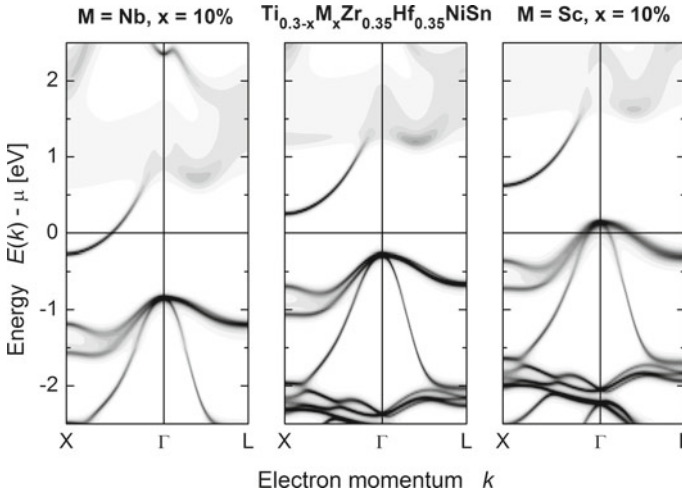
Fig. 10.7 Electronic structure of the n-type $Ti_{0.30}Zr_{0.35}Hf_{0.35}NiSn$ from ab initio calculations performed by Dr. G.H. Fecher at Max-Planck-Institute for Chemical Physics of Solids (Dresden). The Fermi energy is shifted into the conduction band with 10 % Nb substitution and into the valence band with 10 % Sc substitution

conduction bands and the origin of the substituted elements (see Fig. 10.7). Elements with donor dopant properties (elements with more valence electrons) introduce additional electrons into the HH system, leading to a shift of the Fermi energy towards the conduction band (i.e. higher energies) and increasing of the band gap size. Therefore, minority carriers are suppressed and cause a shift of the Seebeck coefficient to higher temperatures. Acceptor dopants (elements with less valence electrons) introduce holes into the system, shift the Fermi energy towards the valence band (to lower energies) and cause a change of the electronic transport from n- to p-type conductivity. Thus, the best n-type HH materials based on the MNiSn system and many of the fairly good p-type HH compounds are based on the MCoSb HH system [32, 64].

Ouardi et al. have shown the impact of acceptor doping in the n-type $Ti_{0.30}Zr_{0.35}Hf_{0.35}NiSn$ HH system [57]. The substitution of 4 % Sc on the Ti-position induced a change in transport properties from n- to p-type conduction, where the Seebeck coefficient α reveals a maximum for both n- and p-type compound at $|\alpha| \approx 210\,\mu VK^{-1}$ at 600 K. Figure 10.7 illustrates the influence of site substitution in the n-type $Ti_{0.30}Zr_{0.35}Hf_{0.35}NiSn$ compound with Nb as a donor dopant and Sc as an acceptor dopant. It can be seen, that electron doping changes the position of the Fermi energy with 10 % Nb substitution into the conduction band, and with 10 % Sc substitution into the valence band. Tobola et al. [65] have shown that the impact on the transport properties via electronic doping in HH materials depends on the sublattice where the substitution takes place. Thus, adding one electron on the Z-site (e.g. Sn replaced by Sb) does not have the same effect as increasing the number of electrons at the X-site by replacing Ti by Nb, due to the different origin

of the electrons and their localization in the DOS. It can be assumed, that a change in the number of electrons on the X-site (Ti replaced by a non-isoelectronic TM) has the greatest influence on the electronic properties, since these elements are responsible for the appearance of the electronic states near the Fermi level [39, 57]. Krez et al. investigated the Hall carrier concentration of the $Ti_{0.3-x}Nb_xZr_{0.35}Hf_{0.35}NiSn$ system [66]. For samples with high Nb content, it could be observed that the carrier concentration remained constant and no intrinsic excitation occurred at high temperatures. The Hall mobility, μ_H decreased with increasing Nb concentration, which may be caused by the scattering of the charge carriers as a result of the additional metal inclusions. The variation in mobility with temperature can be described by a power law equation: $\mu \propto T^{-\nu}$, where the value of ν is an indicator of the most dominant scattering mechanism in the system. For phase-separated HH compounds, Xie et al. were able to show that the major mechanism is alloy scattering [67].

10.4 Phase Separation as a Key to a Thermoelectric High Efficiency

A general challenge in improving HH compounds for thermoelectric applications is the comparatively high thermal conductivity of the order of $10\,WK^{-1}m^{-1}$. In the late 1990 s a common approach to reduce the thermal conductivity was to increase the phonon scattering. Hohl et al. reduced the thermal conductivity by a factor of three for different temperatures by introducing disorder on the X-sites of $X_{0.5}X'_{0.5}NiSn$ (X, X′ = Ti, Zr, Hf) [68, 69]. Substitution of tin by antimony increases both the thermal and electrical conductivities [70]. Substitution at the Ni position also decreases the thermal conductivity [71]. The composition $Zr_{0.5}Hf_{0.5}Ni_{0.8}Pd_{0.2}Sn_{0.99}Sb_{0.01}$ possesses a figure of merit $ZT = 0.7$ at $527\,°C$ [72]. For a long time the TE applicability of HH compounds was limited by their high thermal conductivities $\kappa > 7$–$10\,WK^{-1}m^{-1}$ [73].

But owing to the development in the TE community, the introduction of mass disorder due to site substitution (alloying) [32, 64] and nanostructures [29, 45] is an effective way to produce additional phonon scattering and with it to decrease the thermal conductivity. Thus, the substitution of non- and isoelectronic elements leads to a drastic decline in the thermal conductivity ($\kappa < 4$ W/Km) in HH materials [63]. The resulting higher disorder due to higher mass and strain fluctuations and an intrinsic phase separation in multi-component HH materials are responsible for the strong reduction in κ. Another approach is to implement a nano- or microstructure in the thermoelectric material. This can be achieved by phase separation, composite materials, pulverization with additional spark plasma sintering or by a complex lattice structure [74, 75]. The experimental efforts of site substitution in HH compounds significantly improved the TE performances of HH materials. Hereby, zT values of 1.5 at $427\,°C$ in the n-type $Zr_{0.25}Hf_{0.25}Ti_{0.5}NiSn_{0.998}Sb_{0.002}$ [63, 76] and zT $\approx$ 1 in the p-type $Ti_{0.12}Zr_{0.44}Hf_{0.44}CoSn_{0.8}Sb_{0.2}$ material [64] could be attained.

Fig. 10.8 Light microscope
image of n-type
$Ti_{0.30}Zr_{0.35}Hf_{0.35}NiSn$
compound. The sample was
etched with a
$HCl : HNO_3 : HF : H_2O$
solution to emphasize the
intrinsic phase separation
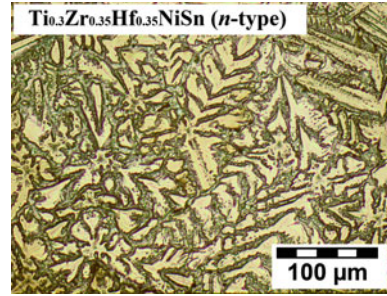
A remarkable characteristic of multi-component HH compounds is their intrinsic
phase separation, shown in Fig. 10.8, when the compounds are solidified by rapid
cooling, leading to a significant reduction of κ, and thus to improved TE efficien-
cies [30]. Sakurada et al. [63] have studied the effect of Ti substitution on the TE
properties in $Ti_x(Zr,Hf)_{1-x}NiSn$. Their results revealed that the thermal conductivity
can be reduced significantly with $x = 0.3$ Ti content to $\kappa \approx 3\,WK^{-1}m^{-1}$ at room
temperature. This strong decline in κ has two origins. First, the high mass strain and
disorder within the $C1_b$ structure due to the Ti substitution at the X-site leads to an
effective phonon scattering. Secondly, this multi-component HH system reveals an
intrinsic phase separation into two HH phases, which provides a further scattering
of phonons at the interfaces.

The eutectic microstructure consists of a main Ti-poor HH 1 phase (bright phase),
which solidifies first and a Ti-rich HH 2 phase (dark phase), which is dendritically
interlaced through the microstructure (see Fig. 10.8). Due to the rapid solidifica-
tion method, small constitutional variations occur in the composition, leading to the
precipitation of small Sn impurities, which are homogenously distributed through-
out the dendritic microstructure with an average size of about 5–10 μm. The com-
position of the two HH phases carried out by electron microscope phase analysis
(EMPA) was found to be $Ti_{0.18}Zr_{0.40}Hf_{0.41}NiSn$ for the Ti-poor HH 1 phase and
$Ti_{0.65}Zr_{0.20}Hf_{0.17}NiSn$ for the Ti-rich HH 2 phase. It seems that Ti is the driving
force of the intrinsic phase separation since the two HH phases differs the most in
the Ti content. The formation of these HH 1 and HH 2 phases is strongly kinetically
favored. Efforts to attain these two HH phases as single phase materials revealed
also phase separations in the sample, resulting from constitutional changes under the
solidification conditions.

The thermal analysis of $Ti_{0.30}Zr_{0.35}Hf_{0.35}NiSn$ carried out by differential scan-
ning calorimetrie (DSC) up to 2000 K in argon gas atmosphere with a heating
rate of 10 Kmin^{-1} is shown in Fig. 10.9a. The DSC curve shows two endothermic
reactions at 1680 K and 1720 K, indicating the eutectic and the melting point of
$Ti_{0.30}Zr_{0.35}Hf_{0.35}NiSn$, respectively. This incongruently melted compound reveals a
strong exothermic recrystallization peak at 1620 K. The supercooling behavior is a
result of the decelerated nucleation in the compound. The melting and recrystalliza-
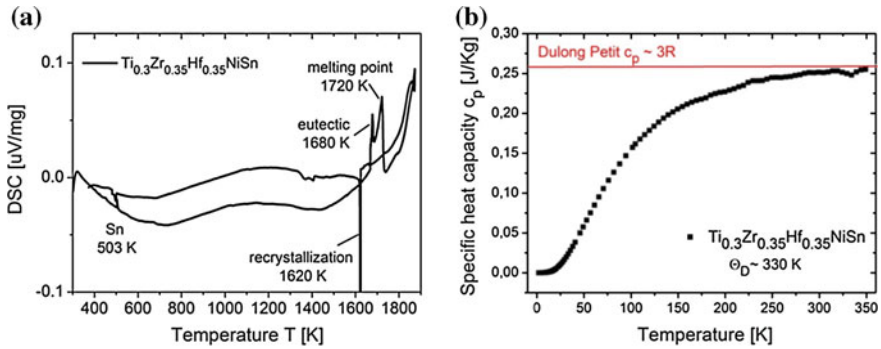tion peaks at about 503 K are caused by Sn impurities in the sample. Specific heat c_p

Fig. 10.9 a DSC measurement of $Ti_{0.30}Zr_{0.35}Hf_{0.35}NiSn$ exemplifies the eutectic temperature at 1680 K and the melting point at 1780 K. The supercooled melt recrystallized at 1680 K. The peaks at 503 K indicate Sn impurities. **b** Specific heat capacity c_p measurement of $Ti_{0.30}Zr_{0.35}Hf_{0.35}NiSn$ compound, indicating the Dulong-Petit limit of $3R$ for Θ_D

measurements of the parent $Ti_{0.30}Zr_{0.35}Hf_{0.35}NiSn$ compound were performed from 10 K to 350 K using a PPMS (see Fig. 10.9b). Since this HH compound has a large number of atoms in the unit cell, many phonon modes appear above room temperature. The Deby temperature was determined to be $\Theta_D = 330$ K. For $T \gg \Theta_D$ the specific heat capacity c_p reached its Dulong-Petit limit of $3R$, corresponding to the value of $c_p \approx 0.26 \, \mathrm{Jg^{-1}K^{-1}}$.

Owing to the high melting points of HH materials the intrinsic phase separation is extraordinary temperature stable and can be considered as the key to high TE efficiencies in HH materials. This leads to the suggestion that temperature stable eutectic microstructures can establish an entirely new area in the TE community, where the phase separation microstructure can be independently engineered to fulfill desired TE properties. For commercial applications, the thermal stability of the phaseseparated microstructure under operating conditions (≈ 873 K in automotive applications) needs to be guaranteed. Therefore, the long-term stability of n- and p-type HH materials based on the $Ti_{0.30}Zr_{0.35}Hf_{0.35}NiSn$-system after 500 cycles (1700 h) from 373 K to 873 K was investigated [77]. The SEM images, shown in Fig. 10.10, revealed the intrinsic phase separation in n-type HH compounds. Surprisingly, the dendritic microstructure showed no obvious change in n-type materials under temperature cycling conditions. The XRD and EMPA results emphasized the extraordinary temperature stability of these HH materials in a moderate temperature range. Due to the high melting point($T \approx 1720$ K) of this (Ti,Zr,Hf)NiSn HH system the resulting phase separation is stable under the given conditions, which is of utmost importance to maintain low thermal conductivities in these HH materials.

The transport properties of the semiconducting n-type $Ti_{0.30}Zr_{0.35}Hf_{0.35}NiSn$ HH system, shown in Fig. 10.11, were measured up to 873 K after 500 cycles (1700 h). The electrical conductivity σ improved after 50 cycles due to an enhancement of the structural order (see Fig. 10.11a). The Seebeck coefficient α is negative at all temperatures, indicating electrons as the majority charge carriers, with a peak value of
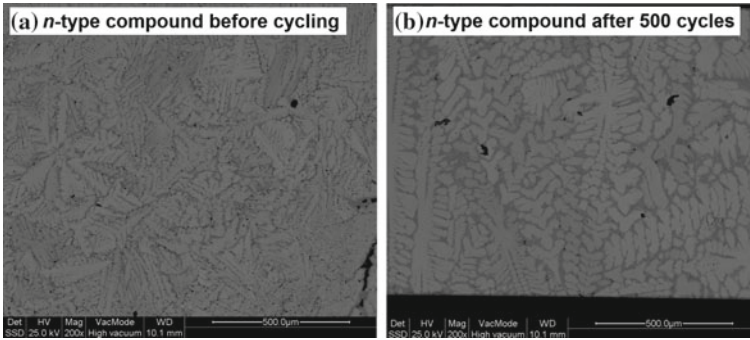
Fig. 10.10 SEM images of the *n*-type $Ti_{0.30}Zr_{0.35}Hf_{0.35}NiSn$ compound before cycling **a** and after 500 cycles (1700 h) from 373 K to 873 K **b**
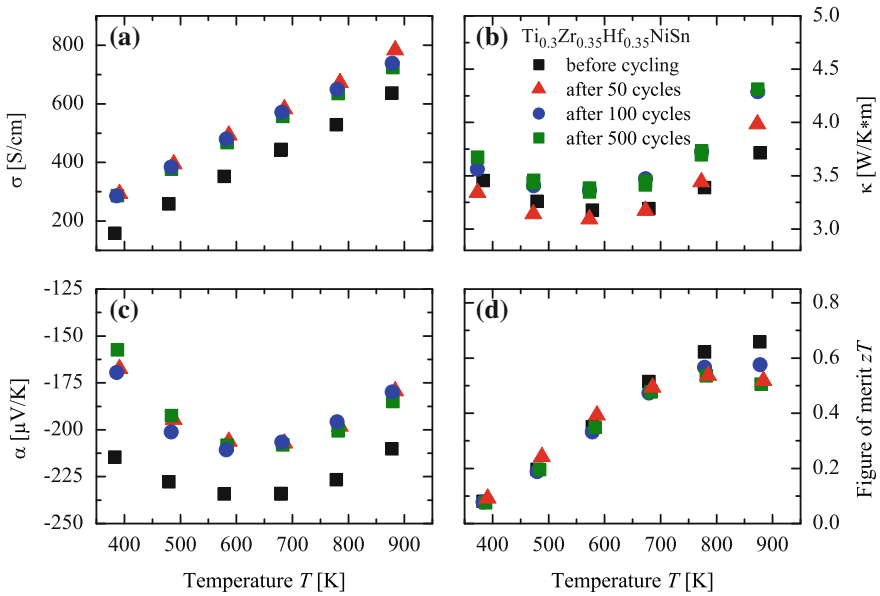

Fig. 10.11 Thermoelectric properties as a function of temperature of the *n*-type $Ti_{0.30}Zr_{0.35}Hf_{0.35}NiSn$ compound under the long-term treatment of 500 cycles. **a** Electrical conductivity $\sigma(T)$. **b** Thermal conductivity $\kappa(T)$. **c** Seebeck coefficient $\alpha(T)$. **d** Figure of merit zT(T)

$\alpha \approx$ -210 μVK^{-1} at 600 K (see Fig. 10.11b). The large Seebeck coefficient emerges from the high density of states, which is caused by the d-states of the transition metals near the Fermi leve [57]. The decrease in α above 600 K is caused by the thermal excitation of intrinsic carries. The power factor PF shows a peak value of 2.5×10^{-3}WK^{-2}m^{-1} at 773 K after 50 cycles, which is comparable to values of n-type Bi$_2$Te$_3$, i.e., $PF \approx 2.6 \times 10^{-3}$WK^{-2}m^{-1} at 423 K [78]. A recent investigation of the long-term efficiency of a commercial available bulk-Bi$_2$Te$_3$ TEG with 31 thermocouples showed a reduction in α and σ caused by material deterioration [79]. The thermal conductivity κ of (Ti,Zr,Hf)NiSn compounds is much than the values of ternary HH alloys, where $\kappa >$ 7-10 WK^{-1}m^{-1} [73]. The low κ values of the phase-separated HH system occur due to different phonon scattering agents in the structure. Owing to the improved structural order of the n-type compound, κ increases slightly after 500 cycles (see Fig. 10.11c). The increase in κ above 600 K is caused by the excitation of intrinsic carriers. The figure of merit zT shows no drastic change after 500 cycles since the values lie within the acceptable error range. This results strongly demonstrate the suitability of phase-separated HH materials, which also comply with requirements such as reproducibility and environmental friendliness via mechanical and thermal stability, for a commercial TE application at moderate temperature.

As already mentoined above, Toshiba (Japan) reported a maximum ZT of 1.5 for Zr$_{0.25}$Hf$_{0.25}$Ti$_{0.5}$NiSn$_{0.998}$Sb$_{0.002}$ at 427 °C [63, 76]. These high ZT values were never reproduced by any other group since the original publication in 2005. In 2013, Schwall and Balke showed that the high Figure of Merit values reported by Shutoh and Sakurada [63, 76] could almost be reproduced (see Fig. 10.12g) [30]. The origin of the exceptional low thermal conductivity is the phase decomposition (see Fig. 10.12a–f), which does not influence the electrical conductivity significantly because of semi-coherent interfaces existing between the three co-existing Heusler phases. These intrinsic properties of the Ti$_{0.5}$Zr$_{0.25}$Hf$_{0.25}$NiSn$_{(1-x)}$M$_x$ | M= Sb, Bi, Te; x= 0-0.006 system show again that the Heusler compounds in matters of the transport properties are competitive thermoelectric materials.

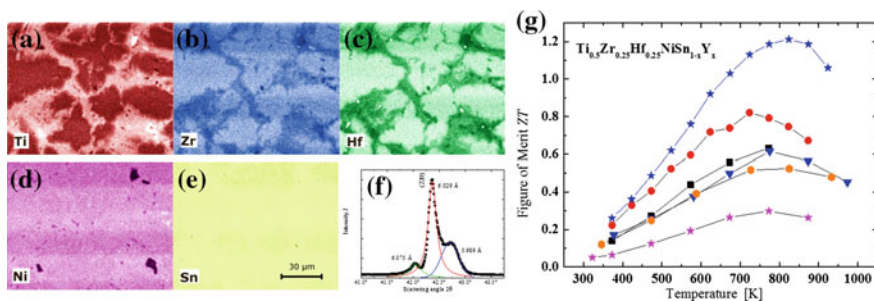**Fig. 10.12** Element-specific EDX mappings of the five constituents of the phase separated Ti$_{0.5}$Zr$_{0.25}$Hf$_{0.25}$NiSn compound with brightness proportional to the concentration **a-e**. (220) reflection of Ti$_{0.5}$Zr$_{0.25}$Hf$_{0.25}$NiSn measured by synchrotron radiation **f**. Temperature dependence of the Figure of Merit of Ti$_{0.5}$Zr$_{0.25}$Hf$_{0.25}$NiSn$_{(1-x)}$M$_x$ compounds **g**

Most of the examined HH materials are n-type semiconductors. As already mentoined above, HH materials can also be p-type semiconductors; XCoSb compounds are the most thoroughly examined p-type systems due to their comparatively high ZT values. Wu et al. reported an iron-doped TiCoSb with the elemental formula $TiFe_{0.3}Co_{0.7}Sb$, that reaches a maximum in ZT of 0.42 at 470 °C. The p-type semiconductors have a thermal conductivity that is 2–3 times higher than the n-type materials and therefore the reduction of the thermal conductivities of the p-type material to the level of the n-type semiconductors, which is nowadays in the range of 3 $WK^{-1}m^{-1}$, seems a very attractive research target with a high technical impact.

Atomic-scale substitution on the various lattice sites of the HH compounds is not the only means to attain increased phonon scattering. Nano-structures at an appropriate scale can also be generated and fine-tuned by suitable thermal treatments, based on a thorough knowledge of the relevant phase diagrams. Disproportionation reactions, as recently shown in multicomponent chalcogenide compounds, while retaining the initial crystal structure of the components, can give rise to nano-structured composites with a reduced thermal conductivity and hence enhanced ZT [80]. Recently, Yan et al. were able to enhance the ZT of p-Type HH compound via a nanostructuring approach [34]. They succeeded in achieving grain sizes smaller than 200 nm in p-type HH samples with a composition of $Zr_{0.5}Hf_{0.5}CoSb_{0.8}Sn_{0.2}$ by ball milling the alloyed ingot into nanopowders and then hot pressing them into dense bulk samples, resulting in a simultaneous increase in Seebeck coefficient and a significant decrease in thermal conductivity, which led to a 60 % improvement in peak ZT from 0.5 to 0.8 at 700 °C.

Using the approach of introducing stronger phonon scattering by larger differences in atomic mass and size in p-type HH compounds $Hf_{1-x}Ti_xCoSb_{0.8}Sn_{0.2}$ Yan et al. were able to increase the ZT to 0.9 at 700 °C [35]. Very recently, it has been shown, that it is possible to introduce an intrinsic phase separation as well in the p-type Heusler system $(Ti/Zr/Hf)CoSb_{0.8}Sn_{0.2}$ and $(Ti/Zr/Hf)CoSb_{0.85}Sn_{0.15}$ analogue to the n-type system [81]. Mandatory is the isoelectronic alloying of Ti with Hf on the Y position, which results in a microstructuring of the material consisting of at least two Heusler phases - one rich in Ti and Sn and another rich in Hf and Sb. The subsequent reduction of the thermal conductivity leads to a maximum ZT of 1.15 at 710 °C [82]. For recent reviews about nanocomposite HH materials see [19, 27, 29].

10.5 Summary

In summary, one can say that the HH compounds fulfill already most of the industrial demands for TE materials, i.e. environment-friendliness, low cost and availability of raw materials, long term stability, processible in industrial production and chemical and mechanical resistance toward high temperatures. The most recent results strongly underline the importance of phase separations as an important tool in the design of highly thermoelectric efficient materials which fulfill the industrial demands for a thermoelectric converter. For achieving the goal of a greater fundamental under-

standing and later on for the sophisticated design of phase separated HH compounds with thermoelectric properties beyond the state of the art one has to clearly separate general effects of nanostructuring from material specific influences and work on a very detailed fundamental investigation of the crystallographic, mechanical, and thermoelectric properties of HH compounds.

References

1. https://flowcharts.llnl.gov/. 2014
2. J. Yang, F.R. Stabler, J. Electron. Mater. **38**, 1245 (2009)
3. K. Schierle-Arndt, W. Hermes, Chemie in unserer Zeit **47**, 92 (2013)
4. T.M. Tritt, Annu. Rev. Mater. Res. **41**, 433 (2011)
5. G.J. Snyder, E.S. Toberer, Nat. Mater. **7**, 105 (2008)
6. P. Ball, T. Caillat, *MRS Bulletin Energy Quarterly, June* Energy Quarterly Thermoelectric Heat Recovery could boots Auto Fule Economy (2011)
7. B.C. Sales, Science **295**, 1248 (2002)
8. J. Yang, T. Caillat, MRS Bull. **31**, 224 (2006)
9. A. Ioffe, *Semiconductor Thermoelements and Thermoelectric Cooling* (Infosearch, London, 1957)
10. A. Ioffe, Sci. Am. **199**, 31 (1958)
11. H. Goldsmid, *Applications of Thermoelectricity*, Methuen's Monographs on Physical Subjects (Methuen, London, 1960)
12. G.S. Nolas, J. Sharp, H.J. Goldsmid, *Thermoelectrics: Basic Principles and New Materials Developments* (Springer, Berlin, 2001)
13. J.R. Sootsman, D.Y. Chung, M. Kanatzidis, Angew. Chem. Int. Ed. **48**, 8616 (2009)
14. L.D. Hicks, M.S. Dresselhaus, Phys. Rev. B **47**, 12727 (1993)
15. L.D. Hicks, M.S. Dresselhaus, Phys. Rev. B **47**, 16631 (1993)
16. G.A. Slack, in *CRC Handbook of Thermoelectrics*, ed. by D.M. Rowe (CRC, 1995), pp. 407–440
17. K. Nielsch, J. Bachmann, J. Kimling, H. Böttner, Adv. Energy Mater. **1**, 713 (2011)
18. G.J. Snyder, Appl. Phys. Lett. **84**, 2436 (2004)
19. W. Liu, X. Yan, G. Chen, Z. Ren, Nano Energy **1**, 42 (2012)
20. Z.-G. Chen, G. Han, L. Yang, L. Cheng, J. Zou, Prog. Nat. Sci.: Mater. Int. **22**, 535 (2012)
21. P. Pichanusakorn, P. Bandaru, Mater. Sci. Eng.: R: Rep. **67**, 19 (2010)
22. H. Alam, S. Ramakrishna, Nano Energy **2**, 190 (2013)

23. W. Jeischko, Metall. Mater. Trans. B **1**, 3159 (1970)
24. H.C. Kandpal, C. Felser, R. Seshadri, J. Phys. D: Appl. Phys **39**, 776 (2006)
25. F. Heusler, Verh. d. DPG **5**, 219 (1903)
26. L.O. Grondahl, S. Karrer, Phys. Rev. Ser. I **33**, 531 (1911)
27. S. Chen, Z. Ren, Mater. Today **16**, 387 (2013)
28. F. Casper, T. Graf, S. Chadov, B. Balke, C. Felser, *Semicond. Sci. Technol.***27** (2012)
29. S.J. Poon, D. Wu, S. Zhu, W. Xie, T.M. Tritt, P. Thomas, R. Venkatasubramanian, J. Mater. Res. **26**, 2795 (2011)
30. M. Schwall, B. Balke, Phys. Chem. Chem. Phys. **15**, 1868 (2013)
31. K. Bartholomé, B. Balke, D. Zuckermann, M. Köhne, M. Müller, K. Tarantik, Jan König, J. Electron. Mater. **43**, 1775 (2014)
32. G. Joshi, T. Dahal, S. Chen, H.Z. Wang, J. Shiomi, G. Chen, Z.F. Ren, Nano Energy **2**, 82 (2013)
33. T. Jäger, C. Mix, M. Schwall, X. Kozina, J. Barth, B. Balke, M. Finsterbusch, Y.U. Idzerda, C. Felser, G. Jakob, Thin Solid Films **520**, 1010 (2011)
34. X. Yan, G. Joshi, W. Liu, Y. Lan, H. Wang, S. Lee, J.W. Simonson, S.J. Poon, T.M. Tritt, G. Chen et al., Nano Lett. **11**, 556 (2011)
35. X. Yan, W. Liu, H. Wang, S. Chen, J. Shiomi, K. Esfarjani, H. Wang, D. Wang, G. Chen, Z. Ren, Energy Environ. Sci. **5**, 7543 (2012)
36. P.H. Ngan, D.V. Christensen, G.J. Snyder, L.T. Hung, S. Linderoth, N.V. Nong, N. Pryds, phys. Status Solidi (a) **211**, 9 (2014)
37. M. Schwall, B. Balke, Appl. Phys. Lett. **98**, 042106 (2011)
38. C.S. Birkel, W.G. Zeier, J.E. Douglas, B.R. Lettiere, C.E. Mills, G. Seward, A. Birkel, M.L. Snedaker, Y. Zhang, G.J. Snyder et al., Chem. Mater. **24**, 2558 (2012)
39. J.W. Simonson, D. Wu, W.J. Xie, T.M. Tritt, S.J. Poon, Phys. Rev. B **83**, 235211 (2011)
40. H. Hazama, M. Matsubara, R. Asahi, J. Electron. Mater. **41**, 1730 (2012)
41. H.-H. Xie, C. Yu, T.-J. Zhu, C.-G. Fu, G.J. Snyder, X.-B. Zhao, Appl. Phys. Lett. **100**, 254104 (2012)
42. M.-S. Lee, F.P. Poudeu, S.D. Mahanti, Phys. Rev. B **83**, 085204 (2011)
43. Y. Gelbstein, N.T.A. Yarmek, Y. Rosenberg, M.P. Dariel, S. Ouardi, B. Balke, C. Felser, M.Köhne, J. Mater. Res. **26** (2011)
44. M. Mikami, Y. Kinemuchi, K. Ozaki, Y. Terazawa, T. Takeuchi, J. Appl. Phys. **111**, 093710 (2012)
45. J.P.A. Makongo, D.K. Misra, X. Zhou, A. Pant, M.R. Shabetai, X. Su, C. Uher, K.L. Stokes, and Pierre F.P. Poudeu, J. Am. Chem. Soc. **133**, 18843 (2011)
46. M.A. Verges, P.J. Schilling, P. Upadhyay, W.K. Miller, R. Yaqub, K.L. Stokes, P.F.P. Poudeu, Sci. Adv. Mater. **3**, 659 (2011)
47. P. Klaer, M. Kallmayer, C.G.F. Blum, T. Graf, J. Barth, B. Balke, G.H. Fecher, C. Felser, H.J. Elmers, Phys. Rev. B **80**, 144405 (2009)
48. P. Klaer, T. Bos, M. Kallmayer, C.G.F. Blum, T. Graf, J. Barth, B. Balke, G.H. Fecher, C. Felser, H.J. Elmers, Phys. Rev. B **82**, 104410 (2010)
49. C. Yu, T. Zhu, K. Xiao, J. Shen, X. Zhao, Funct. Mater. Lett. **03**, 227 (2010)
50. J.E. Garay, Annu. Rev. Mater. Res. **40**, 445 (2010)
51. C.S. Birkel, J.E. Douglas, B.R. Lettiere, G. Seward, N. Verma, Y. Zhang, T.M. Pollock, R. Seshadri, G.D. Stucky, Phys. Chem. Chem. Phys. **15**, 6990 (2013)
52. M. Zou, J.-F. Li, B. Du, D. Liu, T. Kita, J. Solid State Chem. **182**, 3138 (2009)
53. C. Wang, J. Meyer, N. Teichert, A. Auge, E. Rausch, B. Balke, A. Hütten, G.H. Fecher, C. Felser, J. Vac. Sci. Technol. B **32**, 020802 (2014)
54. S. Ouardi, G.H. Fecher, B. Balke, X. Kozina, G. Stryganyuk, C. Felser, S. Lowitzer, D. Ködderitzsch, H. Ebert, E. Ikenaga, Phys. Rev. B **82**, 085108 (2010)
55. S. Ouardi, G.H. Fecher, C. Felser, M. Schwall, S.S. Naghavi, A. Gloskovskii, B. Balke, J. Hamrle, K. Postava, J. Pištora et al., Phys. Rev. B **86**, 045116 (2012)
56. K. Miyamoto, K. Kimura, K. Sakamoto, M. Ye, Y. Cui, K. Shimada, H. Namatame, M. Taniguchi, S.I. Fujimori, Y. Saitoh, E. Ikenaga, K. Kobayashi, J. Tadano, T. Kanomata, Appl. Phys. Express **1**, 081901 (2008)

57. S. Ouardi, G.H. Fecher, B. Balke, M. Schwall, X. Kozina, G. Stryganyuk, C. Felser, E. Ikenaga, Y. Yamashita, S. Ueda et al., Appl. Phys. Lett. **97**, 252113 (2010)
58. D.M. Rowe, *Thermoelectrics Handbook: Macro to Nano* (CRC Taylor & Francis, Boca Raton, 2006)
59. J. Yang, Adv. Funct. Mater. **18**, 2880 (2008)
60. A. Horyn', O. Bodak, L. Romaka, Y. Gorelenko, A. Tkachuk, V. Davydov, Y. Stadnyk, J. Alloy. Compd. **363**, 10 (2004)
61. J.M. Ziman, *Electrons and Phonons* (Oxford University Press, Oxford, 1960)
62. S.R. Culp, J.W. Simonson, S.J. Poon, V. Ponnambalam, J. Edwards, T.M. Tritt, Appl. Phys. Lett. **93**, 022105 (2008)
63. S. Sakurada, N. Shutoh, Appl. Phys. Lett. **86**, 2105 (2005)
64. X. Yan, W. Liu, S. Chen, H. Wang, Q. Zhang, G. Chen, Z. Ren, Adv. Energy Mater. **3**, 1195 (2013)
65. J. Tobola, J. Pierre, S. Kaprzyk, R.V. Skolozdra, M.A. Kouacou, J. Phys. Condens. Matter **10**, 1013 (1998)
66. J. Krez, J. Schmitt, G.J. Snyder, C. Felser, W. Hermes, M. Schwind, *J. Mater. Chem. A* **2**, 13513 (2014)
67. H. Xie, H. Wang, Y. Pei, C. Fu, X. Liu, G.J. Snyder, X. Zhao, T. Zhu, Adv. Funct. Mater. **23**, 5123 (2013)
68. H. Hohl, A. Ramirez, W. Kaefer, K. Fess, Ch. Thurner, Ch. Kloc, E. Bucher, Mater. Res. Soc. Symp. Proc. **478**, 109 (1997)
69. H. Hohl, A. Ramirez, C. Goldmann, G. Ernst, B. Wolfing, E. Bucher, J. Phys.: Condens. Matter **11**, 1697 (1999)
70. S. Öğüt, K.M. Rabe, Phys. Rev. B **51**, 10443 (1995)
71. Q. Shen, L.M. Zhang, L.D. Chen, T. Goto, T. Hirai, J. Mater. Sci. Lett. **20**, 2197 (2001)
72. Q. Shen, L. Chen, T. Goto, T. Hirai, J. Yang, G.P. Meisner, C. Uher, Appl. Phys. Lett. **79**, 4165 (2001)
73. S.R. Clup, S.J. Poon, N. Hickman, T.M. Tritt, J. Blumm, Appl. Phys. Lett. **88**, 042106 (2006)
74. T. Graf, J. Barth, C.G.F. Blum, B. Balke, C. Felser, P. Klaer, H.J. Elmers, Phys. Rev. B **82**, 194420 (2010)
75. T. Graf, P. Klaer, J. Barth, B. Balke, H.J. Elmers, C. Felser, Scr. Mater. **63**, 1216 (2010)
76. S. Sakurada, N. Shutoh, J. Alloy. Compd. **389**, 204 (2005)
77. J. Krez, B. Balke, W. Hermes, M. Schwind, C. Felser, arXiv:1502.01828 (2015)
78. L. Zhao, B.-P. Zhang, W. Liu, H. Zhang, J.-F. Li, J. Alloy. Compd. **467**, 91 (2009)
79. E. Hatzikraniotis, K.T. Zorbas, I. Samaras, Th Kyratsi, K. Paraskevopoulos, J. Electron. Mater. **39**, 2112 (2010)
80. Y. Gelbstein, B. Dado, O. Ben-Yehuda, Y. Sadia, Z. Dashevsky, M.P. Dariel, Chem. Mater. **22**, 1054 (2010)
81. E. Rausch, B. Balke, S. Ouardi, C. Felser, Phys. Chem. Chem. Phys. **16**, 25258 (2014)
82. E. Rausch, S. Ouardi, U. Burkhardt, C. Felser, J.M. Stahlhofen, B. Balke, arXiv:1502.03336 (2015)